MethodsX 13 (2024) 102879

Contents lists available at ScienceDirect

MethodsX

journal homepage: www.elsevier.com/locate/methodsx

Method for computer tomography voxel-based finite element analysis and validation with digital image correlation system ☆,☆☆

Debangshu Paul [a,*], Zachariah Arwood [a], Pierre-Yves Mulon [b], Dayakar Penumadu [a], Timothy Truster [a]

[a] Department of Civil and Environmental Engineering, University of Tennessee, Knoxville, TN 37996, USA
[b] University of Tennessee College of Veterinary Medicine, 2407 River Dr, Knoxville, TN 37996, USA

ARTICLE INFO

Method name:
Quantitative Computed Tomography (QCT) based finite element analysis validated by digital image correlation system

Keywords:
Finite element analysis
Computed tomography
Voxel-based mesh
Phase-field modeling
Spatial density distribution
Nodal property projection
Open source

ABSTRACT

Understanding the mechanical behavior of heterogeneous materials is becoming increasingly crucial across various fields, including aerospace engineering, composite materials development, geology, and biomechanics. While substantial literature exists on this topic, conventional methods often rely on commercial software packages. This study presents a framework for computed tomography (CT) scan-based finite element (FE) analysis of such materials using open-source software in most of the workflow.
Our work focuses on three key aspects:

1. Mesh generation that incorporates spatially varying mechanical properties and well-defined boundary conditions.
2. Validation of the FE results through comparison with digital image correlation (DIC) system measurements.
3. Open-source software utilization throughout the entire process, making it more accessible and cost-effective.

This work aims to demonstrate the effectiveness of this framework for analyzing heterogeneous materials in various fields, offering a more accessible and affordable approach.

Specifications table

Subject area:	Engineering
More specific subject area:	Finite element analysis of heterogeneous material
Name of your method:	Quantitative Computed Tomography (QCT) based finite element analysis validated by digital image correlation system.
Name and reference of original method:	None
Resource availability:	3D slicer: https://www.slicer.org/ GNU Octave, version 4.2.2: http://www.octave.org CloudCompare: https://www.danielgm.net/cc/ MOOSE: https://mooseframework.inl.gov/

☆ **Related research article:** None.
☆☆ **For a published article:** None.
* Corresponding author.
E-mail address: dpaul11@vols.utk.edu (D. Paul).

https://doi.org/10.1016/j.mex.2024.102879
Received 3 June 2024; Accepted 25 July 2024
Available online 3 August 2024

Background

While structural study of homogeneous material is available in literature, and methods for both linear and non-linear finite element (FE) analysis have been well developed, structural analysis of heterogeneous materials with inconsistent density and mechanical properties (i.e., bone, wood etc.) remains a challenge.

Bone has heterogeneous structure and its composition changes with age and different diseases [1]. The mechanical properties of bone, like other structural materials, depend on the composition. Since the composition of a bone is affected by age, different diseases, nutrition, and many other factors, predicting the mechanical behavior of the bone by measuring the bone composition has been central for skeletal studies and very important in orthopedics. Because of such structure, mechanical behavior of bone cannot be predicted with accuracy if the variation of the density throughout the bone is not considered.

Personalized FE models of bones based on quantitative computed tomography (QCT) have been used extensively to estimate bone stiffness and strength. Computed tomography (CT) data consists of single images (slices) of the scanned object, which together comprise a 3D image consisting of voxels, i.e., pixels with a third spatial dimension, whose size is contingent to the scanner resolution. Each voxel is assigned a scalar intensity value corresponding to the measured Hounsfield units (HU) and can be visualized as a greyscale value.

Among musculoskeletal structural studies, human femur [2–4] and humerus [5,6] have attracted significant interest because of their importance for fracture risk prediction [7] due to osteoporosis [8] or other diseases and injuries, optimal management of bony metastases, and more. QCT-based FE (QCTFE) analysis is considered one of the best current techniques for noninvasive assessment of femoral strength [9].

On the other hand, several studies have focused on applying various image analysis methods to detect and reconstruct internal features of wooden logs from CT scans, e.g., the location of the pith, knots, pitch pockets, heartwood, sapwood, and annual rings structures [10–13].

To evaluate the mechanical properties of a material that is heterogeneous and has inconsistent density, it is important to correlate the measured density with the strength [14]. Correlation of apparent density and the stiffness of the heterogeneous material was studied in 1985 [15,16] and later several works were conducted in this field for mapping of the experimentally measured density through assumed model forms to produce local property variations across the specimens [17–20]. To capture the complex geometry as well as local heterogeneous and anisotropic characteristics [21], 3D CT scans were used to obtain the geometry and spatial density distribution.

Despite the extensive published literature on CT scan-based FE modeling, there is a lack of readily available, standardized guidelines for conducting such analyses. This results in researchers new to the field spending a significant amount of time developing frameworks for pre-processing CT data and post-processing the evaluated and measured data. For example, one specific challenge lies in generating a 3D mesh from the CT scan data, particularly when defining side sets where boundary conditions will be applied. These side sets are crucial for specifying how the material will interact with its surroundings in the simulation. Additionally, nodal data from digital imaging and communications in medicine (DICOM) images need to be extracted in a usable format that allows mapping of mechanical properties onto the nodal cloud of the 3D mesh. These nodal properties, such as density or elasticity values assigned to each node, are crucial for predicting the mechanical behavior of the specimen. This paper aims to address this gap by reporting a workflow that can be utilized to create a finite element (FE) model from DICOM files. The workflow will encompass predicting the strain field, post-processing the DIC data to align with the FE mesh, and ultimately validating the model.

The process of building the FE model from the CT scan images (DICOM files) involves different software packages. While there are several commercial software packages available for reading the data from CT scan images, this study developed a methodology to utilize open-source software to map the mechanical properties to the FE model. The open-source software packages that were utilized in the process were 3D Slicer [22,23], MOOSE framework [24], ParaView [25,26] and CloudCompare [27].

Method details

Materials and Methods

To investigate the mechanical properties of complex biological structures, a 3D-printed replica of a goat tibia was employed. A CT scan of the actual bone provided a detailed digital model of its internal structure. This digital model was then translated into a format suitable for 3D printing. Polylactic acid (PLA), a biocompatible plastic material commonly used in 3D printing, served as the printing material for the tibia replica. This approach creates a surrogate for the real bone, allowing for the analysis of various material properties relevant to the goat tibia without harming the original specimen. Additionally, this methodology has the potential to be generalized for analyzing other heterogeneous materials by utilizing their respective CT scan data and appropriate printing materials.

The overarching methodology used herein is summarized as follows:

(1) DICOM images from the CT scan of the 3D printed sample along with phantom tubes were exported as data. This step takes DICOM images as input and creates comma separated value (csv) files with a grid of nodal data.
(2) Phantom tubes were used for calibrating the attenuated data using linear regression.
(3) 3D Slicer, ParaView, and Octave were used to prepare the FE model. A 3D FE mesh was generated by 3D slicer and exported as exodus files which were re-processed using the csv files from step 1 to create a final exodus file with the FE model with spatial properties projected onto the nodes.

Table 1
Mechanical Properties of PLA [28].

Property	Value
Elastic modulus (MPa), E_{PLA}	3500
Poisson's ratio	0.36
Density (mg/cc), ρ_{PLA}	1.252

(4) The FE model was then simulated in the MOOSE framework to determine the displacement and strain field under uniaxial compressive loading. An input file (.i format) was scripted for running the simulation in MOOSE. The results from the simulation were exported as csv and exodus format.
(5) The mechanical experiment was performed using a Materials Test Systems (MTS) servo hydraulic universal testing machine (UTM) (25 kN capacity) with the help of a custom-made metal grip, and a Digital Image Correlation (DIC) system recorded the strain developed on the sample surface. The DIC data was exported as csv files.
(6) The DIC data was post processed using Python scripts.
(7) For calibration and validation of the FE model, the simulation results were compared with the strain field obtained from the DIC data. A combination of CloudCompare, ParaView and Python scripts are used to post process the data.

This workflow is illustrated in Fig. 1.

Modeling approach

The HU values provided by the CT scan need to be correlated with the density of the material to create the FE model. To translate HU values into actual densities, a calibration phantom is often used. This phantom is a physical object with known densities at different points. It is scanned alongside the sample of interest. By comparing the HU values of the phantom to its known densities, a relationship between HU and density can be established. Using the established correlation between HU and density from the calibration phantom, each HU value in the segmented CT scan data is converted to a corresponding density value.

Finally, this density information is incorporated into the nodal cloud of the FE model. Each element in the model is then assigned a stiffness value based on its corresponding density value from the nodes. This allows the FE model to accurately represent the variations in density within the object, leading to more reliable simulations of its mechanical behavior.

QCT of samples and phantom tubes

A total of 703 sequential CT scan slices were made at settings of 120 kV, 170 mA, and slice thickness 0.67 mm. The specimen was encased with PMMA (Poly methyl methacrylate) at the two ends and CT scanned along with the four phantom tubes.

Phantom calibration

The calibration process started with the DICOM images of the goat tibia received from the CT scanner. The property that can correlate to density is denoted as the HU value, which needs to be calibrated to determine the density of the part being scanned. There are several studies on inter-scanner variations [29] and development of methods for calibrating the DICOM images with phantom tubes to measure the density of the bones [30–32]. Following the recommendation of several studies [33], in this work, K_2HPO_4 solution at concentrations of 0 mg/cc, 50 mg/cc, 200 mg/cc and 400 mg/cc are used as the phantom solution and scanned along with the sample (Fig. 2).

Sectra Image viewer [34] was used to analyze the DICOM images and record the HU values (Fig. 3). The HU values of the phantom tubes are used for calibration, and a relationship between the HU value and the mineral density is established. This relation is used during the extraction of nodal properties from the DICOM images (Fig. 3).

Linear regression was applied to fit the following relation between 'apparent solid density' and HU value of the phantom tubes (Fig.4):

$$\rho_{K_2HPO_4} = (0.7398x + 1.7827) \times 10^{-3}\ {}^{mg}/_{cc} \tag{1}$$

here,

x = HU value measure by the CT scan.

This study worked with a 3D-printed replica of the bone where the filament material was PLA. The density and stiffness of the PLA in this bone varies slightly due to manufacturing inaccuracies and other limiting factors. In order to find the stiffness of PLA bone, a linear relation between the density and the stiffness was used in this study. Initial values of solid density and stiffness were taken according to Table 1, and the spatial distribution of the stiffness was evaluated using Eq. (1) and the following linear relationship (Eq. (2)):

$$E_{specimen} = \frac{\rho_{K_2HPO_4}}{\rho_{PLA}} \times E_{PLA} \tag{2}$$

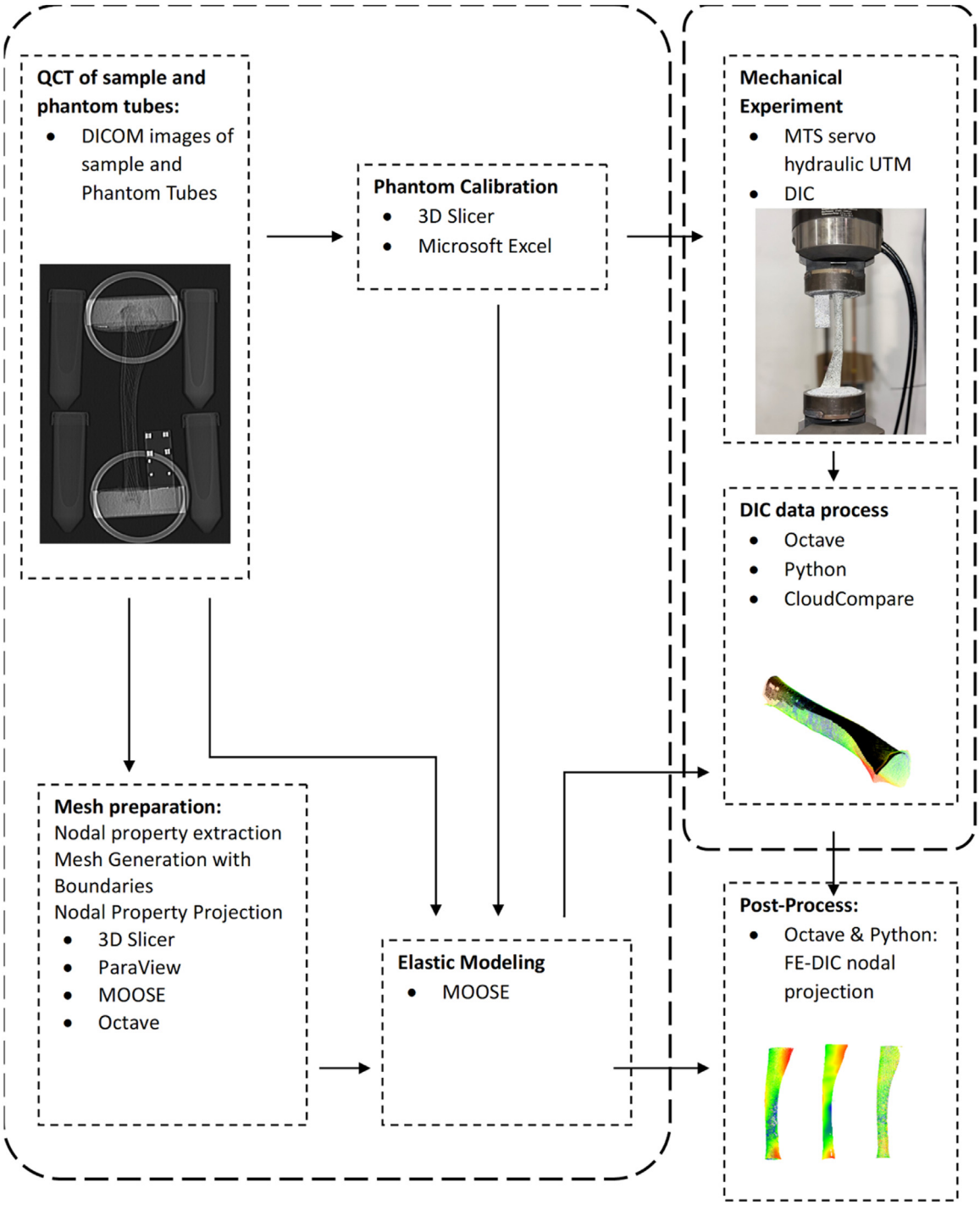

Fig. 1. Methodology framework.

here,

$E_{specimen}$ = Nodal stiffness, and
$\rho_{K_2HPO_4}$ = Nodal apparent density.

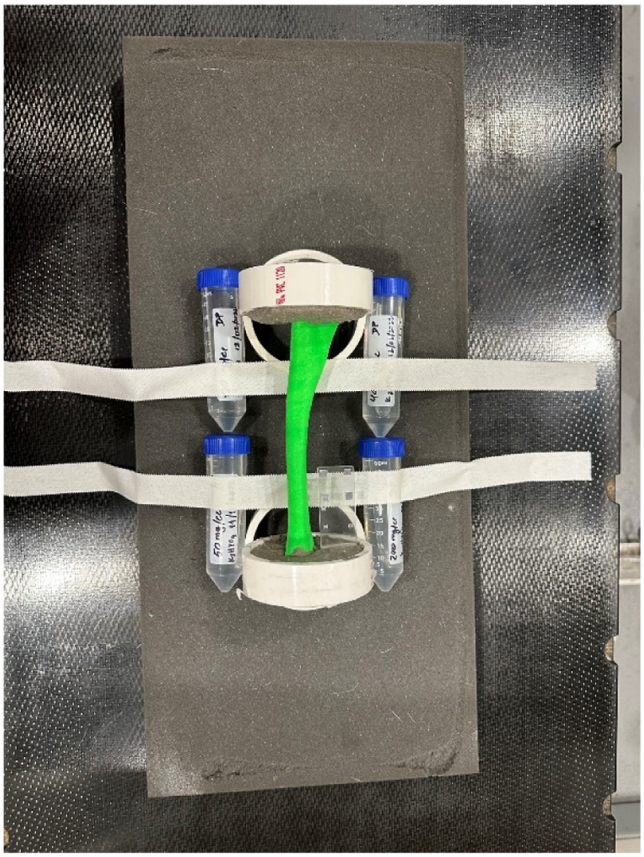

Fig. 2. Specimen with the phantom tubes on the CT scanner bed.

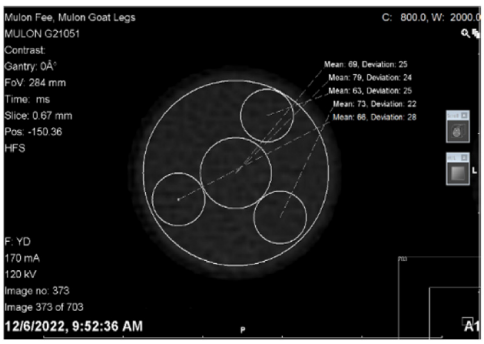

Fig. 3. DICOM images with HU values of phantom tubes (K2HPO4 solution with concentration: 50 mg/cc).

Mesh preparation

Finite element (FE) simulation was employed in this study to predict the mechanical behavior of the material. The FE modeling began with the development of a 3D mesh, which involved several steps.

Nodal property extraction

After the phantom calibration is completed, the calculated nodal stiffness needs to be associated with an FE model. 3D Slicer was used to process the DICOM image. This open-source software was used to a) Extract nodal data, and b) Create FE mesh. Before starting the extraction of nodal data, it was important to verify that the loading axis in the experiment matches the corresponding axis in the DICOM images. While it was challenging due to complex shape of the sample, linear transformation using “transformation” module in 3D slicer was manually utilized to correct any misalignment during the CT scan. The volume was segmented by adjusting

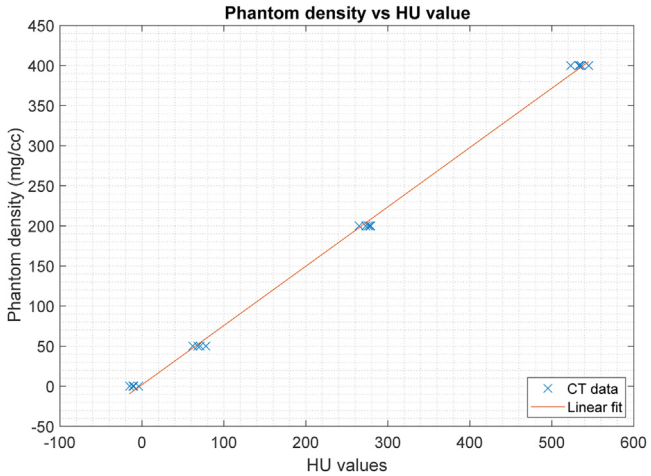

Fig. 4. Phantom Calibration using K2HPO4 solution with concentration: 0 mg/cc, 50 mg/cc, 200 mg/cc, 400 mg/cc).

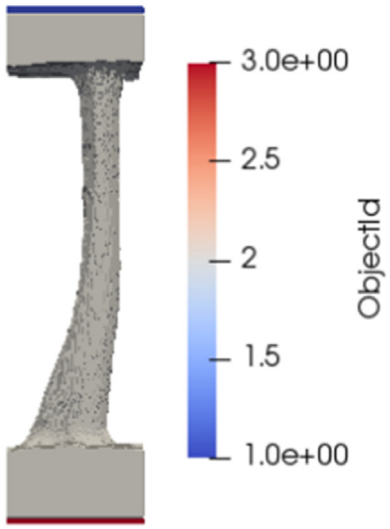

Fig. 5. FE model including top and bottom endcaps that will be used in later calibrations.

thresholds to separate the sample from the air. Some manual polishing of the surface using the "smoothing tool" was required to avoid any sharp discontinuities on the surface that could create convergence issues for FE analysis. A Python script was used with 3D Slicer to extract the nodal properties from the DICOM files. The nodal property was extracted for the whole volume as it gives the flexibility of using an FE interpolation method in later steps.

Mesh generation with boundaries

The segmented parts were converted to a tetrahedral mesh using an open-source module "Segment Mesher" [35] to create the 3D FE mesh. This study used 3 mesh files, where only one will be used for FE analysis and the other two dummy meshes were used for creating the side sets where boundary conditions will be applied (Fig. 5). The two dummy meshes need to cover the extreme ends of the volume so that they can be used for calibrating the nodal projection process. The coordinate axes of the FE mesh generated by the 3D Slicer are different from those of the extracted nodal property grid from the DICOM files. Thus, calibration is required to align and scale the axes before mapping the properties.

Side sets generation

The FE analysis requires side sets on which to apply loads. A combination of ParaView and MOOSE operations were performed to create 2 side sets between the 2 pairs of subdomains. MOOSE is used to create different IDs for the three meshes, and then ParaView stitches them using the "merge blocks" operation. A mesh operation named "SideSetsBetweenSubdomainsGenerator" in

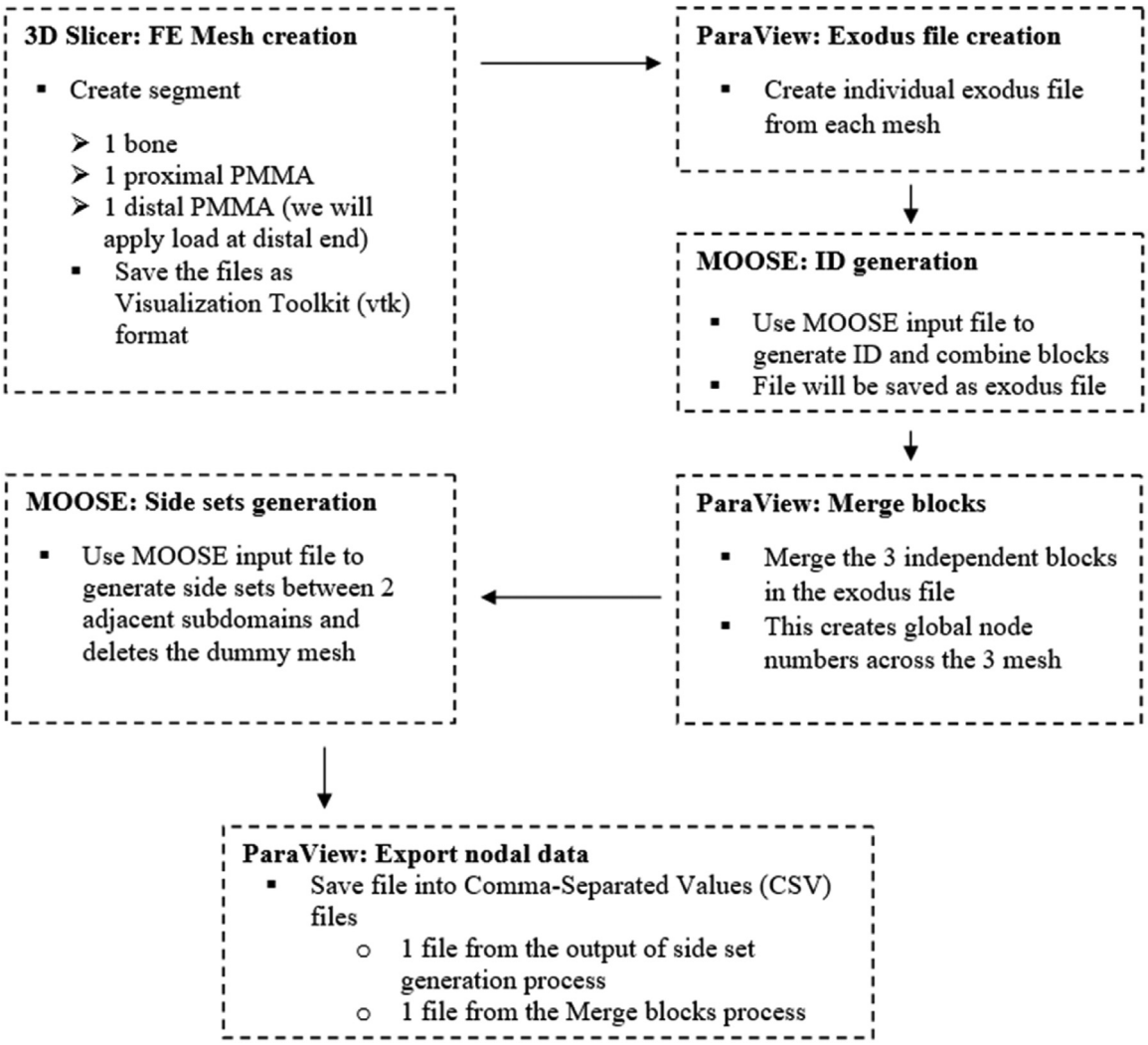

Fig. 6. Workflow to create mesh with boundaries along with corresponding applications utilized.

MOOSE creates side sets between the subdomains which facilitates the application of the boundary conditions. The full workflow of mesh generation can be visualized in Fig. 6.

Nodal property projection

The next step was to build the FE model with stiffness projection to its nodal cloud according to the spatial density distribution of the sample. To map the properties, a FE code was written in Octave to project the properties from the nodal cloud to the nodes in the 3D FE mesh by leveraging structured grids with HU data from DICOM images. These structured grids, with each voxel containing a HU value, provide a well-defined spatial framework for the material properties of the object under study. The FEA script estimates the HU value at any arbitrary point within the nodal cloud of the 3D mesh. The script achieves this by first identifying the closest corners of the 3D cube (voxel) that enclose the target coordinate. A subroutine then interpolates the HU values at these corner voxels to estimate the property value at the desired location. This approach allows the FEA script to incorporate the spatial variations in material properties within the object, leading to more accurate and realistic simulations.

The input files for this code are the multiple nodal coordinate files with associated HU values extracted from 3D slicer, the nodal data extracted from the full material and endcap mesh, and the nodal data extracted from the final mesh using ParaView. First, it reads in the x, y, and z locations from the data extracted from 3D Slicer and locates the HU value assigned to each position. Next, it interpolates the HU values extracted from the DICOM images onto coordinates of the FE model. The axes from the DICOM images do not match the axes from the FE mesh generated by the “Segment Mesher” module. As a result, the script performs a few operations to scale and align the axes properly before the projection. The difference between the axes of DICOM images and FE mesh is not very

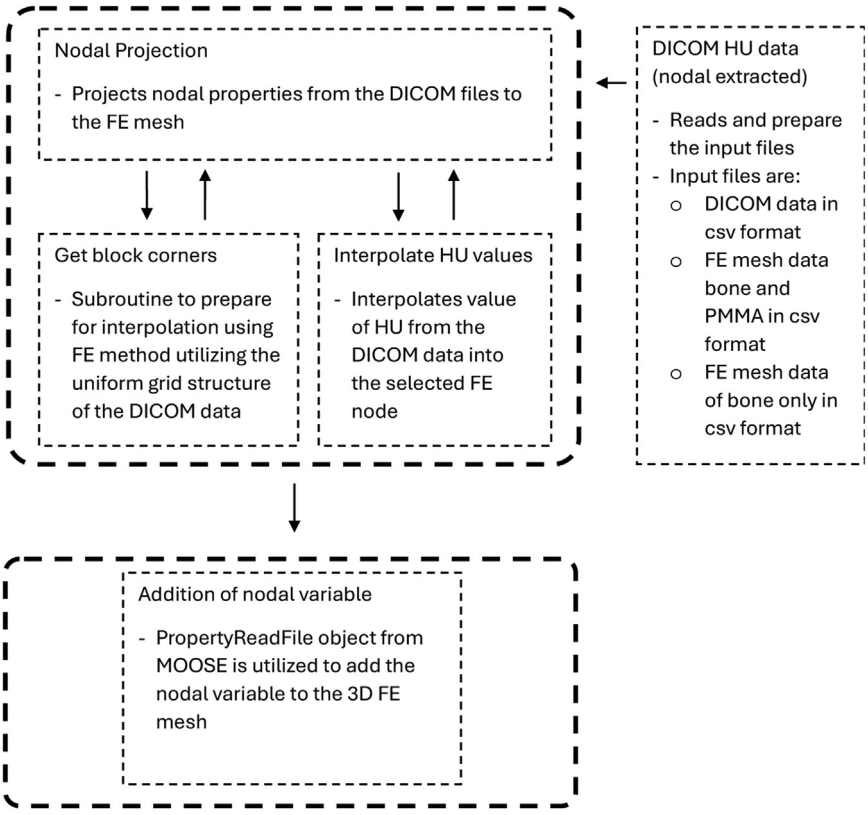

Fig. 7. Algorithm for nodal property projection.

consistent with a small variation of translations in one or more axes. So, the alignment process needs to be fine-tuned manually in the Octave script for each model.

Nodal property mapping

Another set of Octave scripts are used to interpolate the nodal properties from the DICOM data to 3D FE mesh, and the PropertyReadFile object from MOOSE is used to add the spatial density into the FE mesh as a nodal variable. The final output file from this process is a single exodus file that contains the projected HU values onto the 3D model nodal coordinates. Fig. 7 illustrates a full outline of the nodal property projection script.

Automated pre-process

As the process has several repetitive steps if opted for a parametric study or while fine-tuning the model, a shell script was written to automate the main steps:

1. Side set generation
2. Nodal projection
   - Calibrate and align the CT scan and natural axes.
   - Taking the .vtk files as inputs.
   - Taking the csv files from nodal property extraction as inputs.
   - Use a FE interpolation method to project the spatial density into the FE mesh.
3. Addition of nodal variable
   - Add the projected property into the FE mesh.

Elastic modeling

The FE model was then simulated in the MOOSE framework to determine the displacement and strain field under uniaxial compressive loading. The goal of this simulation is to visualize the displacement and strain field produced during uniaxial compressive loading. The input file contained a ParsedMaterial object that relates the spatial stiffness with the density distribution. A ParsedMaterial object takes the function expression as an input parameter in the form of a function parser expression. The nodal variable from the final exodus file generated in the previous step was used as a SolutionUserObject and the properties are parsed to generate

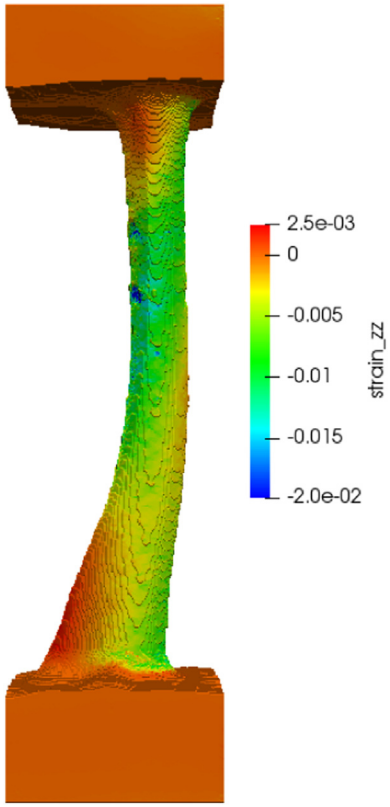

Fig. 8. Contour of strain along the shaft axis of the sample under axial compression.

elemental variables for the simulation. After the simulation is complete, MOOSE outputs an exodus file containing the displacement and strain data. In this study, a displacement of 1 mm was used. The strain fields can be observed in ParaView (Fig. 8).

Method validation

Mechanical experiment

The 3D-printed PLA goat tibia was then prepared as a specimen for mechanical testing to compare with the FE simulation result. The two ends were encased in PMMA with 6-inch diameter PVC rings as supports. Two custom-made metal adapters were fabricated to house the PVC-PMMA ends and facilitate the MTS (25 kN capacity) servo-hydraulic UTM to grip the specimen. The specimen was prepared for the DIC system with white paint and black speckles (Fig. 9). A displacement rate of 1 mm/min was applied until the specimen failed and data was collected from the MTS and DIC for post processing (Fig. 10).

A glass slide was embedded into the PMMA at the end where the UTM applies the displacement to serve two purposes: (1) To help with the alignment of the DIC data and the FE mesh from the CT data by providing a flat surface in the nodal cloud; (2) To become a reference plane attached to the top PMMA support/base/grip that rigidly translates during the experiment to provide a reference displacement for the moving grip.

The three-dimensional DIC method was used to ascertain spatially distributed displacement along the PLA bone surface during quasi-static compression loading in accordance with [36]. Images were captured via Vic Snap software *in situ* at 3 Hz frame rate using a dual camera system. Sony IMX174 2.3 megapixel grasshopper cameras equipped with 17 mm Schneider Kreuznach Citrine 1.4/17 compact lenses set at f-stop value of 5.6 (f-stop working range is 1.4–11) were mounted upon a rigid frame at a standoff distance of 0.33 m, with a baseline separation of 76 mm and a stereo angle of 14 degrees for *in situ* imaging. Each camera had a pixel size of 5.86 microns and 1920 × 1200 pixel resolution. The region of interest (ROI) scale was determined as 8.6 pixel/mm in a field of view approximately 223 mm by 140 mm.

Stereo calibration was performed using Correlated Solutions 9 mm 12 × 9 dot calibration target to achieve a calibration score of 0.35, which is within the acceptable range. Data correlation was performed utilizing Vic3D software with a subset size of 33 pixels and a step size of 6 pixels, producing 7335 distinct correlation points with less than 0.035 pixel deviation off the epi-polar line. The subset shape function used was the fixed function in Vic 3D software package, and a filter size of 15 pixels was used data for smoothing. Lagrange strain was extracted for coordinate directions based upon the bone orientation.

Fig. 9. 3D printed part encased in PMMA and prepared for DIC measurement.

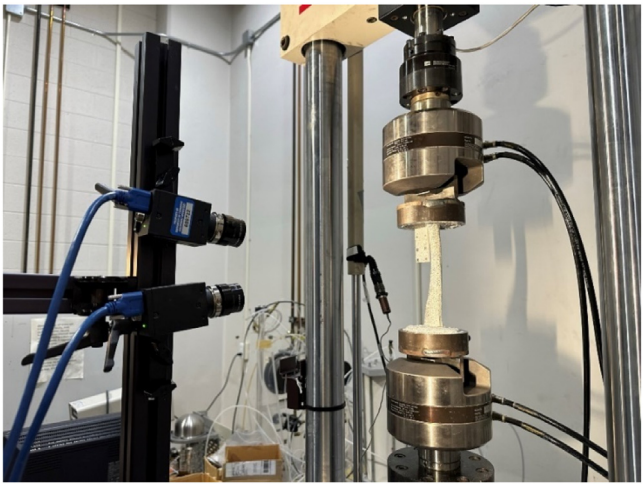

Fig. 10. Mechanical setup for compression loading of the part with DIC system.

Experimental data process

The experimental data were post processed to observe the force vs displacement relation (Fig. 11). A point from the elastic zone was taken to compare with the FE simulation data. The DIC data was processed to get the strain field of that specific point. Displacement applied at that point was used in the FE simulation in this study. A displacement of 1 mm was used for the simulation, and DIC image at that displacement was the corresponding experimental data.

Before processing DIC data, 6 random points were taken on the reference plane to get the displacement value and perform a sanity check of how the DIC data matched the MTS data after aligning the initial time (Fig. 12). The displacement of the 6 random points being on the same line confirms that there was no signification rotation of the reference plane.

Error mapping

CloudCompare has tools to align the mesh automatically by tracing the similar pattern in different point clouds. However, DIC point clouds are from the surface of the region of interest whereas the FE mesh has the point clouds of the total bone with the PMMA at the distal and proximal ends. Additionally, due to resolution of the CT scan and some artifacts generated during the segmentation process in 3D Slicer, some surface features from the FE model and the DIC surface do not match. As a result, the automatic operation in CloudCompare could not be used in this study. Both the FE data and DIC data were imported to CloudCompare, and the DIC point cloud was translated and rotated manually to align the FE mesh (Fig. 13).

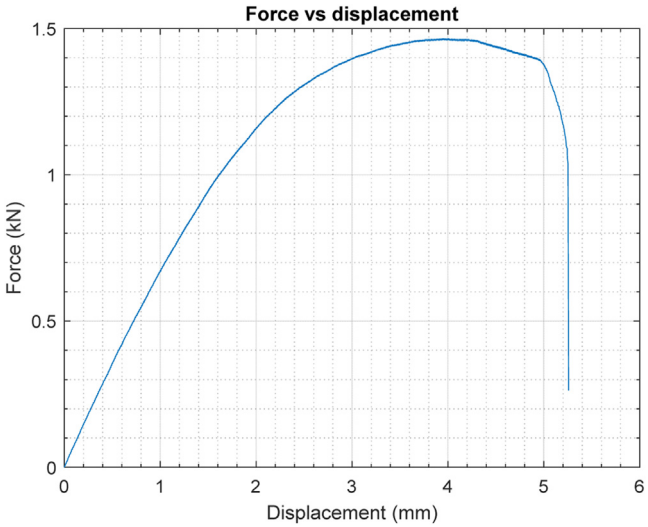

Fig. 11. Force vs Displacement curve from MTS.

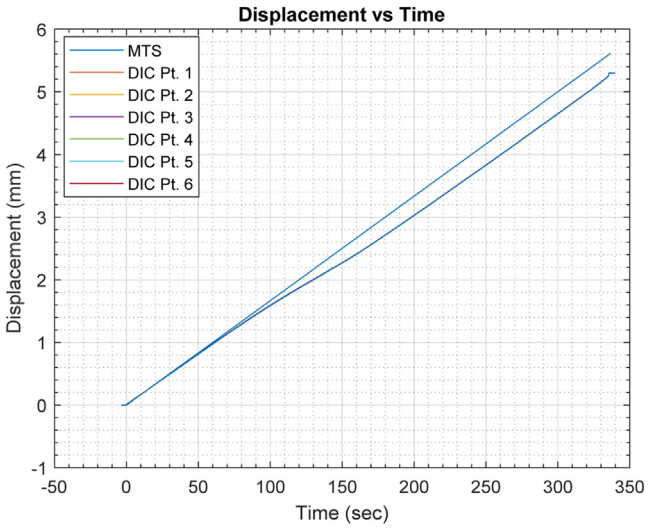

Fig. 12. Displacement vs Time to align MTS and DIC data.

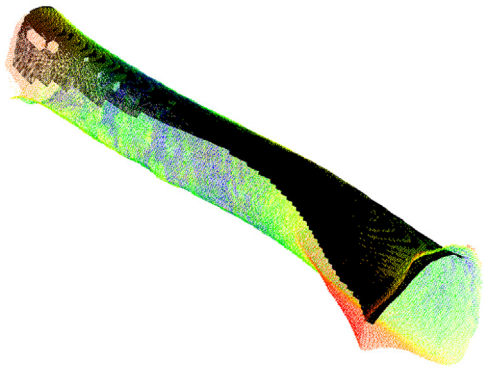

Fig. 13. Aligned FE mesh (RGB) with DIC surface point cloud (Black).

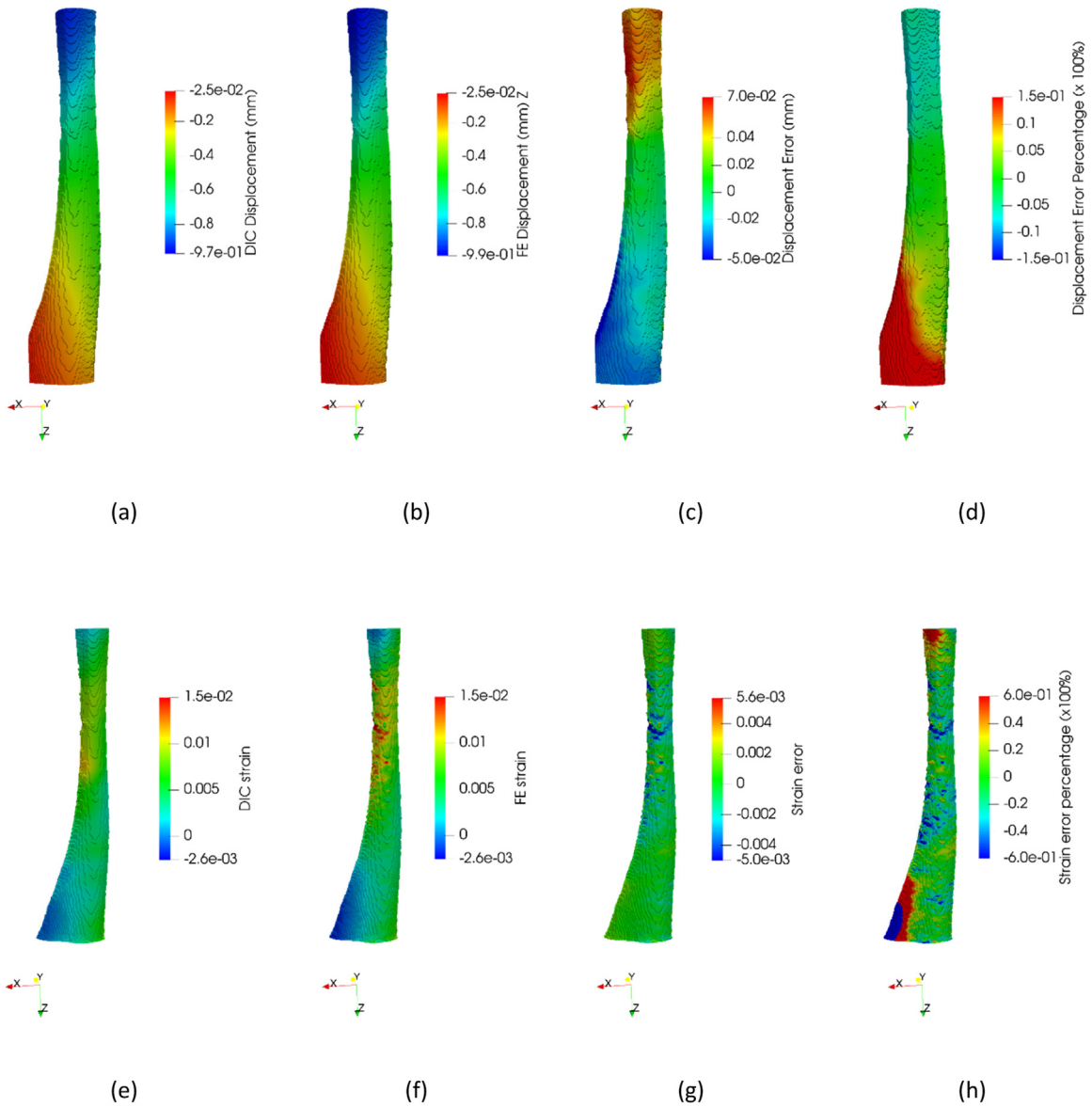

Fig. 14. DIC and FE result comparison (a) DIC displacement, (b) FE displacement, (c) Displacement error, (d) Displacement error percentage, DIC and FE result comparison, (e) DIC strain, (f) FE strain, (g) Stain error, (h) Strain error percentage.

Finally, a number of Octave and Python scripts, which were modified from the nodal projection script, were used to project the DIC data onto the FE mesh. To interpolate the scalar value (strain or displacement) at a specific FE node, the K-Nearest Neighbors (KNN) search in Python was employed. This technique identified the 5 closest points within the DIC nodal cloud, and their corresponding scalar values were used for the interpolation. A contour with the error value was visualized in ParaView. The visual comparison of the DIC and FE data demonstrated that the elastic model predicted the strain field with some deviations near the edges. The error contour illustrates a range of error from -5 % to 7 % for displacement and -15 % to 15 % for strain within a major portion of the region of interest (Fig. 14). The scale was capped to visualize the error mapping in a convenient way. Due to the polishing of DICOM images during segmentation in 3D Slicer, noise in the form of nodes were introduced in the 3D mesh, which do not physically exist, hence have insignificant stiffness values assigned to them. As a result, these nodes contribute strain values that have a higher error value.

Discussion

A methodology was developed that can be used to investigate investigates the mechanical properties of complex materials with unknown qualities. DIC can provide detailed strain field measurements on the actual material sample. This experimental data becomes

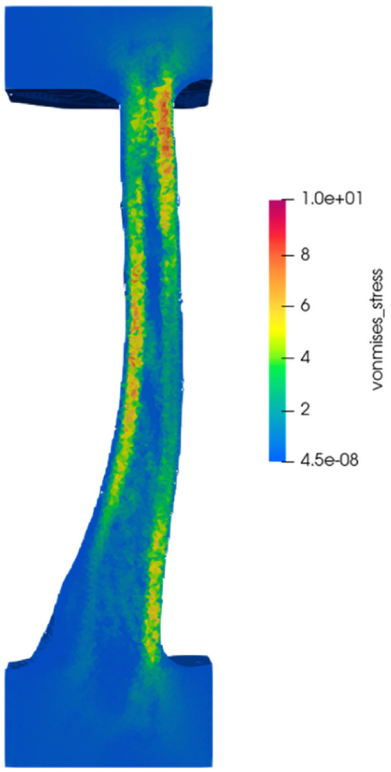

Fig. 15. Von Mises stress generated in the specimen.

the foundation for comparison. An FE model, built using an initial guess for the material's stiffness, simulates the material's behavior under load. The software then predicts the resulting strain field. Researchers can then visualize and quantify the discrepancies between the simulated and real-world behavior by comparing the DIC-derived strain field with the FE model's prediction. These discrepancies highlight areas where the model deviates from reality.

By iteratively adjusting a key parameter in the model and re-running the analysis, researchers can potentially identify a correction factor that minimizes the observed discrepancies. This refined model then allows for estimating the base stiffness of the unknown material by matching the predicted reaction force with the one measured during the actual experiment.

The aim of the study was to develop a method to study heterogeneous materials using CT. This method can be used to analyze structural behavior (only an elastic model was studied in this paper) and evaluate the effective mechanical properties of materials with uncertain spatial density and stiffness distribution.

The first challenge of the method was to project the nodal densities measured in the form of HU values obtained by CT scan onto the FE mesh generated from the DICOM images. As the sample was irregular in size and to develop a method that can work with non-planar boundaries, a combination of steps was used to create the appropriate boundaries. The sample was loaded in an MTS servo hydraulic UTM and loaded to failure. The strain field was measured by a DIC system and compared with the strain field evaluated by the elastic model.

The error plot confirms that the model is working with an accuracy ranging from -5 % to 7 % for displacement and -15 % to 15 % for strain. The base stiffness E_{PLA} is adjusted so that the reaction force on the fixed end calculated by the FE model matches the value measured experimentally.

With the base stiffness confirmed, the elastic model can be used to study other mechanical behaviors (Fig. 15) or perform other analyses coupling with the elastic model (i.e. fracture model, plastic model etc.).

While the literature is rich in studies on QCTFE, analysis of heterogeneous material can be challenging without an established method or framework. The process can be expensive in terms of resources as the methods available in literature depend largely on commercial software and developing an open source-based methodology can be a lengthy process. The method that has been developed in this study can open the door to accessible and affordable research in multi-disciplinary areas such as bone modeling and other musculoskeletal studies.

Limitations

There are some issues to consider regarding this method while preparing for further studies:

a. CT scan machine
   i. The resolution was 0.67 mm for the slices, which affects the accuracy of the process.
   ii. Using micro-CT would reduce the error in the spatial density of the part resulting in greater accuracy of the model. However, it is not likely feasible for such a large-scale model with heterogeneous structure.
b. Segmentation process
   i. The contrast between the material and the environment is important for automatic segmentation in 3D Slicer. Additionally, the resolution and accuracy of the CT scan causes sharp and discontinuous surfaces during the segmentation process, which need to be polished using the smoothing tool. While this contributes to the convergence of the FE analysis, negligible stiffness assigned to those physically non-existent nodes (in the DICOM images) causes unrealistically high strains. With higher resolution of the CT scan machine and contrast between the material and the environment, this issue could be eliminated.
c. Irregular geometry and density distribution
   i. The irregular geometry of the specimen poses the challenge of properly aligning the PMMA-PVC rings, which causes a small offset between the shaft axis and the applied displacement.
   ii. The two ends were fixed to avoid motion in any other direction than the axial or vertical motion. However, the inherent density distribution of the specimen causes it to have small rotation which is observed as torque in the MTS data. The torque was not reported as it was not of significant value. A model considering the torque and reaction force in lateral directions will be more robust and accurate.
d. DIC system
   i. The 2-camera DIC system is limited by the depth of field when measuring out of plane motion, resulting in noise and error at the edges and in the middle of the ROI when dealing with out of plane motion caused by buckling and rotation. A DIC system that can capture the out of plane motion can minimize this limitation.
e. Computational power
   i. While a micro-CT would reduce the error in spatial distribution, it would significantly increase the computational time with an exceptionally enormous number of nodal grid data which is used during nodal property projections. However, with the employment of high performance computing system and proper resource allocation, micro-CT can be used for the investigation.
f. Validation of the method
   i. While the simulation results were compared with the experimental data, and a good agreement was observed, verifying and validating the process with a known homogeneous material before a study will improve the accuracy and reliability of the analysis.

Ethics statements

None

Declaration of competing interest

The authors declare that they have no known competing financial interests or personal relationships that could have appeared to influence the work reported in this paper.

CRediT authorship contribution statement

Debangshu Paul: Methodology, Software, Validation, Investigation, Data curation, Writing – original draft, Visualization. **Zachariah Arwood:** Investigation, Writing – review & editing. **Pierre-Yves Mulon:** Resources, Writing – review & editing. **Dayakar Penumadu:** Resources. **Timothy Truster:** Conceptualization, Writing – review & editing, Supervision, Funding acquisition.

Data availability

Data associated with this article can be found at https://doi.org/10.5281/zenodo.13208901.

Acknowledgment

None.

Supplementary materials

Supplementary material associated with this article can be found at https://doi.org/10.5281/zenodo.13208901.

References

[1] A.L. Boskey, Bone composition: relationship to bone fragility and antiosteoporotic drug effects, BoneKEy Rep. 2 (2013) Dec., doi:10.1038/bonekey.2013.181.
[2] E. Dall'Ara, B. Luisier, R. Schmidt, F. Kainberger, P. Zysset, D. Pahr, A nonlinear QCT-based finite element model validation study for the human femur tested in two configurations *in vitro*, Bone 52 (1) (2013) 27–38 Jan., doi:10.1016/j.bone.2012.09.006.
[3] J. Hazrati Marangalou, K. Ito, B. Van Rietbergen, A new approach to determine the accuracy of morphology–elasticity relationships in continuum FE analyses of human proximal femur, J. Biomech. 45 (16) (2012) 2884–2892 Nov., doi:10.1016/j.jbiomech.2012.08.022.
[4] J.H. Keyak, T.S. Kaneko, J. Tehranzadeh, H.B. Skinner, Predicting proximal femoral strength using structural engineering models, Clin. Orthop. NA (437) (2005) 219–228 Aug., doi:10.1097/01.blo.0000164400.37905.22.
[5] G. Dahan, O. Safran, Z. Yosibash, Can neck fractures in proximal humeri be predicted by CT-based FEA? J. Biomech. 136 (2022) 111039 May, doi:10.1016/j.jbiomech.2022.111039.
[6] L. Hug, G. Dahan, S. Kollmannsberger, E. Rank, Z. Yosibash, Predicting fracture in the proximal humerus using phase field models, J. Mech. Behav. Biomed. Mater. 134 (2022) 105415 Oct., doi:10.1016/j.jmbbm.2022.105415.
[7] B. Helgason, et al., Development of a balanced experimental–computational approach to understanding the mechanics of proximal femur fractures, Med. Eng. Phys. 36 (6) (2014) 793–799 Jun., doi:10.1016/j.medengphy.2014.02.019.
[8] Z. Yosibash, R. Padan, L. Joskowicz, C. Milgrom, A CT-based high-order finite element analysis of the human proximal femur compared to *in-vitro* experiments, J. Biomech. Eng. 129 (3) (2007) 297–309 Jun., doi:10.1115/1.2720906.
[9] T.M. Keaveny, et al., Femoral bone strength and its relation to cortical and trabecular changes after treatment with PTH, alendronate, and their combination as assessed by finite element analysis of quantitative CT scans, J. Bone Miner. Res. 23 (12) (2008) 1974–1982 Dec., doi:10.1359/jbmr.080805.
[10] K. Entacher, et al., Pith detection on CT-cross-section images of logs: an experimental comparison, in: Proceedings of the 2008 3rd International Symposium on Communications, Control and Signal Processing, St. Julian's, Malta, IEEE, 2008, pp. 478–483, doi:10.1109/ISCCSP.2008.4537273. Mar..
[11] E. Johansson, D. Johansson, J. Skog, M. Fredriksson, Automated knot detection for high speed computed tomography on Pinus sylvestris L. and Picea abies (L.) Karst. using ellipse fitting in concentric surfaces, Comput. Electron. Agric. 96 (2013) 238–245 Aug., doi:10.1016/j.compag.2013.06.003.
[12] A. Krähenbühl, B. Kerautret, I. Debled-Rennesson, F. Longuetaud, F. Mothe, Knot detection in X-ray CT images of wood, in: Advances in Visual Computing, 7432, Springer Berlin Heidelberg, Berlin, Heidelberg, 2012, pp. 209–218, doi:10.1007/978-3-642-33191-6_21. G. Bebis, R. Boyle, B. Parvin, D. Koracin, C. Fowlkes, S. Wang, M.-H. Choi, S. Mantler, J. Schulze, D. Acevedo, K. Mueller, and M. Papka, Eds., in Lecture Notes in Computer Science, vol. 7432..
[13] F. Longuetaud, et al., Automatic knot detection and measurements from X-ray CT images of wood: A review and validation of an improved algorithm on softwood samples, Comput. Electron. Agric. 85 (2012) 77–89 Jul., doi:10.1016/j.compag.2012.03.013.
[14] B. Helgason, et al., The influence of the modulus–density relationship and the material mapping method on the simulated mechanical response of the proximal femur in side-ways fall loading configuration, Med. Eng. Phys. 38 (7) (2016) 679–689 Jul., doi:10.1016/j.medengphy.2016.03.006.
[15] R.J. McBroom, W.C. Hayes, W.T. Edwards, R.P. Goldberg, A.A. White, Prediction of vertebral body compressive fracture using quantitative computed tomography, J. Bone Jt. Surg. 67 (8) (1985) 1206–1214 Oct., doi:10.2106/00004623-198567080-00010.
[16] E. Schileo, et al., An accurate estimation of bone density improves the accuracy of subject-specific finite element models, J. Biomech. 41 (11) (2008) 2483–2491 Aug., doi:10.1016/j.jbiomech.2008.05.017.
[17] J.H. Keyak, J.M. Meagher, H.B. Skinner, C.D. Mote, Automated three-dimensional finite element modelling of bone: a new method, J. Biomed. Eng. 12 (5) (1990) 389–397 Sep., doi:10.1016/0141-5425(90)90022-F.
[18] J.H. Keyak, M.G. Fourkas, J.M. Meagher, H.B. Skinner, Validation of an automated method of three-dimensional finite element modelling of bone, J. Biomed. Eng. 15 (6) (1993) 505–509 Nov., doi:10.1016/0141-5425(93)90066-8.
[19] C.M. Les, J.H. Keyak, S.M. Stover, K.T. Taylor, A.J. Kaneps, Estimation of material properties in the equine metacarpus with use of quantitative computed tomography, J. Orthop. Res. 12 (6) (1994) 822–833 Nov., doi:10.1002/jor.1100120610.
[20] R. Shen, H. Waisman, Z. Yosibash, G. Dahan, A novel phase field method for modeling the fracture of long bones, Int. J. Numer. Methods Biomed. Eng. 35 (8) (2019) Aug., doi:10.1002/cnm.3211.
[21] K. Ün, A. Çalık, Relevance of inhomogeneous–anisotropic models of human cortical bone: a tibia study using the finite element method, Biotechnol. Biotechnol. Equip. 30 (3) (2016) 538–547 May, doi:10.1080/13102818.2016.1154803.
[22] "3D Slicer image computing platform, 2024 3D Slicer. Accessed: Mar. 27, 2023. [Online]. Available: https://slicer.org/
[23] A. Fedorov, et al., 3D Slicer as an image computing platform for the Quantitative Imaging Network, Magn. Reson. Imaging 30 (9) (2012) 1323–1341 Nov., doi:10.1016/j.mri.2012.05.001.
[24] G. Giudicelli, et al., 3.0 - MOOSE: Enabling massively parallel multiphysics simulations, SoftwareX 26 (2024) 101690 May, doi:10.1016/j.softx.2024.101690.
[25] J. Ahrens, B. Geveci, C. Law, ParaView: An end-user tool for large-data visualization, in: Visualization Handbook, Elsevier, 2005, pp. 717–731, doi:10.1016/B978-012387582-2/50038-1.
[26] U. Ayachit, The ParaView Guide: A Parallel Visualization Application, Kitware, Inc., Clifton Park, NY, USA, 2015.
[27] CloudCompare. (2023). [GPL software]. Available: http://www.cloudcompare.org/
[28] S. Farah, D.G. Anderson, R. Langer, Physical and mechanical properties of PLA, and their functions in widespread applications — A comprehensive review, Adv. Drug Deliv. Rev. 107 (2016) 367–392 Dec., doi:10.1016/j.addr.2016.06.012.
[29] Y. Katz, G. Dahan, J. Sosna, I. Shelef, E. Cherniavsky, Z. Yosibash, Scanner influence on the mechanical response of QCT-based finite element analysis of long bones, J. Biomech. 86 (2019) 149–159 Mar., doi:10.1016/j.jbiomech.2019.01.049.
[30] C.E. Cann, H.K. Genant, Precise measurement of vertebral mineral content using computed tomography, J. Comput. Assist. Tomogr. 4 (4) (1980) 493–500 Aug., doi:10.1097/00004728-198008000-00018.
[31] A. Nazarian, B.D. Snyder, D. Zurakowski, R. Müller, Quantitative micro-computed tomography: A non-invasive method to assess equivalent bone mineral density, Bone 43 (2) (2008) 302–311 Aug., doi:10.1016/j.bone.2008.04.009.
[32] P. Ruegsegger, W.A. Kalender, A phantom for standardization and quality control in peripheral bone measurements by PQCT and DXA, Phys. Med. Biol. 38 (12) (1993) 1963–1970 Dec., doi:10.1088/0031-9155/38/12/018.
[33] G. Dahan, N. Trabelsi, O. Safran, Z. Yosibash, Finite element analyses for predicting anatomical neck fractures in the proximal humerus, Clin. Biomech. 68 (2019) 114–121 Aug., doi:10.1016/j.clinbiomech.2019.05.028.
[34] "Imaging IT solutions that lead the way in customer satisfaction, 2024 Sectra Medical. Accessed: Mar. 14, 2024. [Online]. Available: https://medical.sectra.com/
[35] H. Si, TetGen, a delaunay-based quality tetrahedral mesh generator, ACM Trans. Math. Softw. 41 (2) (2015) Feb., doi:10.1145/2629697.
[36] E.M.C. Jones, M.A. Iadicola, A Good Practices Guide for Digital Image Correlation, International Digital Image Correlation Society, 2018, doi:10.32720/idics/gpg.ed1.